3356 *Chem. Mater.* **2009,** *21,* 3356–3369
DOI:10.1021/cm901345h

CHEMISTRY OF MATERIALS
Article

Structural Characterization of a Nanocrystalline Inorganic−Organic Hybrid with Fiberlike Morphology and One-Dimensional Antiferromagnetic Properties

Igor Djerdj,*[,†] Minhua Cao,*[,‡,§] Xavier Rocquefelte,[⊥] Radovan Černý,[#] Zvonko Jagličić,[||,¶] Denis Arčon,[□,△] Anton Potočnik,[□] Fabia Gozzo,[○] and Markus Niederberger[†]

[†]*Swiss Federal Institute of Technology (ETH) Zürich, Department of Materials, Wolfgang-Pauli-Strasse 10, CH-8093 Zürich, Switzerland,* [‡]*Max Planck Institute of Colloids and Interfaces, Colloid Department, Research Campus Golm, D-14424 Potsdam, Germany,* [§]*Department of Chemistry, Beijing Institute of Technology, Beijing 100081, P. R. China,* [⊥]*Institut des Matériaux Jean Rouxel, UMR 6502 CNRS-Université de Nantes, 2 rue de la Houssinière, BP 32229, 44322 Nantes, France,* [#]*Laboratory of Crystallography, University of Geneva, 24 quai Ernest Ansermet, 1211 Geneva 4, Switzerland,* [||]*Institute of Mathematics, Physics and Mechanics, University of Ljubljana, Jadranska 19, 1000 Ljubljana, Slovenia,* [¶]*Faculty of Civil and Geodetic Engineering, University of Ljubljana, Jamova 2, 1000 Ljubljana, Slovenia,* [□]*Institute Jožef Stefan, Jamova 39, 1000 Ljubljana, Slovenia,* [△]*Faculty of Mathematics and Physics, University of Ljubljana, Jadranska 19, 1000 Ljubljana, Slovenia, and* [○]*Swiss Light Source, Paul Scherrer Institute, 5232 Villigen, Switzerland*

Received May 15, 2009. Revised Manuscript Received June 4, 2009

A new nanocrystalline inorganic−organic hybrid compound, $VO(C_6H_5COO)_2$ has been synthesized under solvothermal conditions by reacting vanadium(V) oxytriisopropoxide with benzoic acid in toluene. A detailed investigation of the composition, structure and properties of $VO(C_6H_5COO)_2$ using chemical and thermal analysis, synchrotron X-ray powder diffraction, electron microscopy techniques including SEM, TEM and SAED, spectroscopy techniques like XPS, EDX and FTIR, SQUID magnetometry and EPR is carefully described. Due to the low-crystallinity of the final material, its crystal structure has been solved from synchrotron X-ray powder diffraction data by combining a direct space global optimization technique and DFT geometry optimization and subsequently refined by the constraint Rietveld method. The compound crystallizes in the monoclinic system with $a = 20.652(3)$, $b = 6.798(1)$, $c = 9.954(1)$ Å, $\beta = 92.145(6)°$, space group $C2$, and $Z = 4$. The inorganic part of the structure can be regarded as staggered V−V−V chains, formed of corner-sharing VO_6 octahedra, running along the monoclinic b-axis. A strong V−O bond alternation along the chain was evidenced by the DFT geometry optimization. The organic part is based on two crystallographically independent singly ionized benzoate moieties linked to vanadium atoms through a bidentate bridging mode. The morphology of $VO(C_6H_5COO)_2$ exhibits long nanofibers, which further consist of smaller individual nanofibers aligned in parallel to the growth direction along the b-axis, as expected from the 1D nature of the compound. The magnetic susceptibility and X-band EPR measurements shows that the magnetic properties of $VO(C_6H_5COO)_2$ can be described by a $S = 1/2$ linear antiferromagnetic chain model with the isotropic interaction between nearest neighbors and an estimated magnetic spin exchange parameter of $J = -189$ K. DFT calculations have also been carried out to simulate the optical response and to estimate the magnetic spin exchange related to $VO(C_6H_5COO)_2$. Such calculations allowed explaining the yellow-green color of the powder and the one-dimensional character of the magnetic structure.

Introduction

Since the discovery of carbon nanotubes (CNTS),[1] one-dimensional (1D) nanostructures have attracted considerable attention because they represent the smallest objects for efficient transport of electrons and excitons, and thus are especially attractive building blocks for hierarchical assembly of functional nanoscale structures.[2,3] In the case of inorganic materials, such as oxides, nitrides, carbides, chalcogenides, and so forth, 1D morphologies are now quite common. Another important class of materials are hybrid inorganic−organic framework materials defined as compounds that contain both inorganic and organic moieties.

*Corresponding authors. E-mail: igor.djerdj@mat.ethz.ch (I.D.); caomh@bit.edu.cn (M.C.).

(1) Iijima, S. *Nature* **1991**, *354*, 56–58.

(2) Duan, X. F.; Huang, Y.; Cui, Y.; Wang, J. F.; Lieber, C. M. *Nature* **2001**, *409*, 66–69.

(3) Tans, S. J.; Verschueren, A. R. M.; Dekker, C. *Nature* **1998**, *393*, 49–52.

Published on Web 07/01/2009
© 2009 American Chemical Society

A subclass of hybrid materials is metal-organic frameworks (MOF), which is based on metal ions coordinated by polydentate bridging organic ligands.[4−7] Depending on the type of metal ion connectors (chemical element, oxidation state), the end functional group of organic ligands, coordination polyhedra around metal cations, and the conformation of carbon chains, a variety of topological structures, such as one-dimensional (1D) chains,[8] two-dimensional (2D) layers or grids,[9−11] and three-dimensional (3D) porous motifs,[12] can be tailored. In contrast to MOFs, which are characterized by isolated metal atoms linked by multifunctional organic ligands, inorganic−organic hybrid compounds contain infinite metal−oxygen−metal arrays as part of their structure.[13] A crucial point in obtaining inorganic−organic hybrids with desired properties is the ability to control the formation of a particular network through the appropriate choice of the constituent metal and bridging organic linkers. Hybrid inorganic−organic materials have been widely used in gas storage,[6] catalysis,[4] nonlinear optics,[14] magnetism,[15] and molecular recognition and separations.[7] Switching to the nanometric dimensions one enters into the field of nanocrystalline inorganic−organic hybrids, which is a challenging task for bioapplications, i.e., because of their tunable nature, these materials might have potential interest in a variety of imaging, biosensing, biolabeling, and drug delivery applications.[16−18] Moreover, their physical properties might be significantly different compared to the corresponding bulk as one normally expects from the surface effects as well as the quantum confinement of surface-state electrons, surface spins, and other nanoscale related physical phenomena. Including an anisotropic morphology and downgrading to 1D nanostructures, the complexity of such inorganic−organic hybrids becomes higher and the corresponding chemical, optical, electrical, and magnetic properties depart even further from those of the bulk, making thus the research object highly interesting.[19,20]

Considering the electronic structure, theoretical calculations have suggested that inorganic−organic hybrids are semiconductors or insulators with band gaps between 1.0 and 5.5 eV. Because the highest occupied valence bands are dominated by the contribution of the 2p atomic orbitals of carbon atoms of the aromatic rings with a small contribution of the atoms from the carboxylate groups, changing the degree of conjugation in the ligands should provide a way to tune the bandgaps.[12] Moreover, by proper design and realization of inorganic−organic hybrids, particularly by the proper choice of the metal ion or even by doing a partial substitution of metal ions of one type with another one, it is possible to tune the band gaps ranging from semiconducting (insulating) to metallic states, which significantly broadens the application possibility of inorganic−organic hybrids.[21]

In the last several years, we have shown that the so-called nonaqueous sol−gel routes are valuable alternatives to aqueous systems. Nonaqueous sol−gel syntheses gave access to a large variety of binary and ternary metal oxide nanoparticles,[22−24] oxide-based inorganic−organic hybrids,[25,26] metal (oxide) hydroxides,[27,28] and doped metal oxides.[29−31] The obtained inorganic nanoparticles exhibit phase purity as-obtained, high crystallinity without further post-thermal treatment, and last but not least, a tunable morphology. Further extension of the nonaqueous sol−gel route to the field of nanocrystalline inorganic−organic hybrids with reduced dimensionality is a fascinating task, particularly with respect to achieving additional interesting physical properties. Such an approach would not result in single crystals, which is often the prerequisite for the successful solving of the crystal structure, but in an additional challenge (powder XRD, DFT-based geometry optimization) to reveal new crystal structures of nanopowders.

Herein, we report a one-step nonaqueous chemical synthesis of a novel nanocrystalline inorganic−organic hybrid that is identified as vanadium oxobenzoate exhibiting a complex morphology, consisting of long nanofibers where many of them comprises several smaller nanofibers. The synthesis is based on a nonaqueous process involving the reaction of vanadium(V) oxytriisopropoxide with benzoic acid in toluene at elevated

(4) Seo, J. S.; Whang, D.; Lee, H.; Jun, S. I.; Oh, J.; Jeon, Y. J.; Kim, K. *Nature* **2000**, *404*, 982–986.
(5) Rosi, N. L.; Eckert, J.; Eddaoudi, M.; Vodak, D. T.; Kim, J.; O'Keeffe, M.; Yaghi, O. M. *Science* **2003**, *300*, 1127–1129.
(6) Yaghi, O. M.; O'Keeffe, M.; Ockwig, N. W.; Chae, H. K.; Eddaoudi, M.; Kim, J. *Nature* **2003**, *423*, 705–714.
(7) Kosal, M. E.; Chou, J. H.; Wilson, S. R.; Suslick, K. S. *Nat. Mater.* **2002**, *1*, 118–121.
(8) Okuda, K.; Hata, H.; Date, M. *J. Phys. Soc. Jpn.* **1972**, *33*, 1574–1580.
(9) Ouellette, W.; Yu, M. H.; O'Connor, C. J.; Zubieta, J. *Inorg. Chem.* **2006**, *45*, 7628–7641.
(10) Choi, J. W.; Park, J. J.; Park, M.; Moon, D. Y.; Lah, M. S. *Eur. J. Inorg. Chem.* **2008**, 5465–5470.
(11) Gu, Y. B.; Yang, M. H. *Cryst. Res. Technol.* **2008**, *43*, 1331–1334.
(12) Tachikawa, T.; Choi, J. R.; Fujitsuka, M.; Majima, T. *J. Phys. Chem. C* **2008**, *112*, 14090–14101.
(13) Rao, C. N. R.; Cheetham, A. K.; Thirumurugan, A. *J. Phys.: Condens. Matter* **2008**, *20*, 083202.
(14) Evans, O. R.; Lin, W. B. *Acc. Chem. Res.* **2002**, *35*, 511–522.
(15) Mahata, P.; Sen, D.; Natarajan, S. *Chem. Commun.* **2008**, 1278–1280.
(16) Descalzo, A. B.; Martinez-Manez, R.; Sancenon, F.; Hoffmann, K.; Rurack, K. *Angew. Chem., Int. Ed.* **2006**, *45*, 5924–5948.
(17) Rieter, W. J.; Taylor, K. M. L.; Lin, W. *J. Am. Chem. Soc.* **2007**, *129*, 9852–9853.
(18) Taylor, K. M. L.; Jin, A.; Lin, W. *Angew. Chem., Int. Ed.* **2008**, *47*, 7722–7725.
(19) Sanchez, C.; Lebeau, B.; Chaput, F.; Boilot, J. P. *Adv. Mater.* **2003**, *15*, 1969–1994.
(20) Holder, E.; Tessler, N.; Rogach, A. L. *J. Mater. Chem.* **2008**, *18*, 1064–1078.
(21) Choi, J. H.; Choi, Y. J.; Lee, J. W.; Shin, W. H.; Kang, J., K. *Phys. Chem. Chem. Phys.* **2009**, *11*, 628–631.
(22) Niederberger, M. *Acc. Chem. Res.* **2007**, *40*, 793–800.
(23) Pinna, N.; Niederberger, M. *Angew. Chem., Int. Ed.* **2008**, *47*, 5292–5304.
(24) Mutin, P. H.; Vioux, A. *Chem. Mater.* **2009**, *21*, 582–596.
(25) Pinna, N.; Garnweitner, G.; Beato, P.; Niederberger, M.; Antonietti, M. *Small* **2005**, *1*, 112–121.
(26) Pinna, N. *J. Mater. Chem.* **2007**, *17*, 2769–2774.
(27) Djerdj, I.; Sheptyakov, D.; Gozzo, F.; Arcon, D.; Nesper, R.; Niederberger, M. *J. Am. Chem. Soc.* **2008**, *130*, 11364–11375.
(28) Djerdj, I.; Garnweitner, G.; Su, D. S.; Niederberger, M. *J. Solid State Chem.* **2007**, *180*, 2154–2165.
(29) Clavel, G.; Willinger, M. G.; Zitoun, D.; Pinna, N. *Adv. Funct. Mater.* **2007**, *17*, 3159–3169.
(30) Djerdj, I.; Arcon, D.; Jaglicic, Z.; Niederberger, M. *J. Solid State Chem.* **2008**, *181*, 1571–1581.
(31) Djerdj, I.; Garnweitner, G.; Arcon, D.; Pregelj, M.; Jaglicic, Z.; Niederberger, M. *J. Mater. Chem.* **2008**, *18*, 5208–5217.

temperature. Besides the novelty of the resulting product, we present an original approach in the crystal structure solution and refinement performed by combining a direct space method (global optimization) followed by a Rietveld refinement of the starting model, deduced from the powder synchrotron XRD, with DFT-based geometry optimization. Apart from the thorough structural characterization of the final product including SEM, TEM, XPS, elemental analysis, TGA, SAED, FTIR, and Raman spectroscopy, ab initio calculations have been done in order to reveal the electronic structure of the new inorganic−organic hybrid. Finally, the magnetic properties of such 1D magnet were probed by DC magnetization and EPR measurements and compared to DFT calculated properties in order to obtain a clear picture of the investigated material.

Experimental Section

Materials. Vanadium(V) oxytriisopropoxide, benzoic acid (99.5%), and toluene (99.8%, anhydrous) were obtained from Aldrich and used without further purification. The heat treatment was performed in Parr acid digestion bombs with 45 mL Teflon cups.

Synthesis. All procedures were started in a glovebox (O_2 and H_2O < 0.1 ppm). In a typical synthesis of nanofibers, 1 mmol of vanadium(V) triisopropoxide and 3 mmol of benzoic acid were added to 20 mL of anhydrous toluene under vigorous stirring. The transparent reaction solution of yellow color was transferred into the autoclave. The autoclave was taken out of the glovebox and heated at 200 °C for 48 h in a regular laboratory furnace. The resulting suspension was centrifuged, and the precipitate was thoroughly washed with ethanol and dried at 60 °C in air for 1 day. The final product was ground in a mortar to yield a yellow-green powder.

Characterization. Scanning electron microscopy (SEM) measurements were performed on a LEO 1550 Gemini with a gold-coated sample. Transmission electron microscopy (TEM) measurement was performed on a Zeiss EM 912Ω instrument at an acceleration voltage of 120 kV, while high-resolution transmission electron microscopy (HRTEM) characterization was performed on a CM30ST microscope (Philips; LaB_6 cathode, operated at 300 kV, point resolution of 2 Å). For TEM characterization, the nondried sample which stayed suspended in ethanol after the washing procedure was thoroughly sonicated. One drop of this suspension was placed on a 400-mesh carbon-coated copper grid and left in air to dry. Thermal stability of the material was probed by the thermogravimetric analysis (TGA), which was performed on Netzsch TG 209 F1 at a scanning rate of 20 °C/min under an air atmosphere. The elemental analysis was performed on a Perkin-Elmer 2400 element analyzer and inductively coupled plasma (ICP) analysis on a Perkin-Elmer Optima 3300DV ICP spectrometer. The oxidation state of vanadium was determined by X-ray photoelectron spectroscopy (XPS), using an ESCALAB 250 spectrometer. The density of the powder was determined at 20 °C using a gas-penetration pycnometer AccuPyc 1330 operating with He gas. IR spectrum of the polycrystalline material was recorded on a FT-IR Bruker 66v spectrometer under a vacuum with KBr pelletized sample.

High-resolution X-ray powder diffraction patterns were collected at the Swiss Light Source powder diffraction station using the multicrystal analyzer detector.[32] The powder was mounted in a 0.5 mm Lindemann capillary and the capillary span at approximately 10 Hz. In order to keep changes induced by radiation under control, multiple short diffraction patterns (15 min) were collected under identical conditions, carefully inspected and merged into a single pattern if no sign of radiation damage was detected. The photon beam wavelength calibration was performed using the NIST silicon standard (640C) mounted in a 0.5 mm Lindemann capillary. A Rietveld refinement has given the value $\lambda = 1.034693 \pm 0.000024$ Å.

Bulk DC magnetic properties have been studied with a QUANTUM DESIGN MPMS-XL-5 SQUID magnetometer. Magnetization M as a function of temperature T has been measured between 2 and 300 K in several constant magnetic fields (100, 1000, and 10 000 Oe). In addition the isothermal magnetization M versus magnetic field strength H at temperature of 2 K was obtained. As the $M(H)$ curve at $H = 1000$ Oe is still linear, we calculated the susceptibility $\chi = M/H$ from $M(T)$ measurements. The susceptibility data are corrected for a small diamagnetic contribution of the sample holder and for the diamagnetic contribution of the inner core electrons obtained from the Pascal tables ($\chi_{dia} = -1.7 \times 10^{-4}$ emu/mol).[33] X-band continuous wave (cw) EPR measurements were performed on a commercial Bruker E580 spectrometer using TE102 dual cavity and Oxford cryogenics continuous flow E900 cryostat. The temperature stability was better than ±0.2 K over the entire temperature range.

Structure Solution and Refinement. The observed first 14 reflections of $VO(C_6H_5COO)_2$ were indexed with the autoindexing program WDICVOL04.[34] The solution with figure of merit [M(14) = 15.9, F(14) = 44.6(0.0123, 20)] has been chosen between monoclinic solutions which indexed all selected peaks. A *C*-centered monoclinic cell was found ($a = 20.652(3)$, $b = 6.798(1)$, $c = 9.954(1)$ Å, $\beta = 92.145(6)°$) with no other observable systematic extinctions. The structure was solved in the space group *C*2 using the program FOX[35] and direct space method. On the basis of the measured density (1.560(3) g cm^{-3}) and observed cell volume the structure was modeled with one rigid octahedron VO_6 and two independent rigid benzoate molecules $C_6H_5COO^-$ kept in a flat conformation. The same correct solution was identified in several global optimization runs of around 1 h each.

The structural model was refined with the Rietveld method by using the program TOPAS.[36] The intermediate solution of the Rietveld refinement was used as a starting model which was further DFT geometry optimized. Output data of the geometry optimization were finally introduced again in the Rietveld refinement through restraint of the bonds and angles yielding to the final structural model. The benzoate molecules were described as semirigid bodies using the internal coordinates (Z-matrix). The phenyl ring of both benzoate molecules was kept flat, and only the torsion angle between C1 and C2 was allowed to vary within the limit −30 to +30° and the C−C and C−O distances within the limit 1.2−1.5 Å. Then the position and orientation of the molecules were allowed to vary. The V−O

(32) Gozzo, F.; Schmitt, B.; Bortolamedi, T.; Giannini, C.; Guagliardi, A.; Lange, M.; Meister, D.; Maden, D.; Willmott, P.; Patterson, B. P. *J. Alloys Compd.* **2004**, *362*, 206–217.
(33) Kahn, O. Molecular Magnetism; VCH Publishers: Weinheim, Germany, 1993.
(34) Boultif, A.; Louer, D. *J. Appl. Crystallogr.* **2004**, *37*, 724–731.
(35) Favre-Nicolin, V.; Černý, R. *J. Appl. Crystallogr.* **2002**, *35*, 734–743.
(36) Coelho, A. A. TOPAS-Academic, **2004**, http://members.optusnet.com.au/~alancoelho.

distance restraints of 2 Å for four vanadium coordinating oxygens of the benzoate molecules and of 1.87 Å for the two remaining oxygens (one independent site O3) were used to model the VO_6 octahedron. Three isotropic displacement parameters (vanadium, carbon and oxygen atoms) were refined. The diffraction profiles were described by the pseudo-Voigt function, and the background (the relatively high background is due to the high amorphous content visible in HRTEM images) by the Chebyshev polynomials. The observed anisotropic line broadening was supposed to be due to the anisotropic crystallite size and was described by a spherical harmonics model. In the final run, 39 structural, 4 lattice parameters, 14 profile, and 19 background parameters were allowed to vary. The uncertainties of the atomic parameters of the carbon and oxygen atoms from the benzoate molecules were not available from the least-squares matrix, because the molecules were refined using their internal coordinates and were therefore estimated by the bootstrap method.[37]

Ab Initio Calculations. Density functional theory (DFT) calculations have been carried out using two different codes: the Vienna Ab initio Simulation Program (VASP) for the geometry optimization of the structures and the WIEN2k program package for the calculation of the electronic structures and the spin exchange parameters and the simulation of the optical properties.[38,39]

To correctly describe the spin state of V^{4+} ions (d^1 electronic configuration), the resulting local structure, and its related properties (electronic, magnetic and optical), we have carried out DFT calculations within the generalized gradient approximation (GGA)[40] plus on-site Coulomb repulsion (U). The validity of the GGA+U approach has been tested by changing the value of the effective Hubbard parameter, $U_{eff} = U - J$. As it will be discussed in the next section, a U_{eff} value of about 2 eV has been shown to provide a coherent picture of the magnetic and optical properties of $VO(C_6H_5COO)_2$.

The parameters used in the VASP calculations are the following. The wave functions are expanded in a plane-wave basis set with kinetic energy below 500 eV. The VASP package is used with the projector augmented wave (PAW) method of Blöchl.[41] The integration in the Brillouin Zone is done by the Methfessel-Paxton method[42] on a set of k-points determined by the Monkhorst-Pack scheme.[43] All the optimizations of atomic coordinates are driven by following a conjugate gradient minimization of the total energy scheme (3.10−2 eV/Å). During the optimization the lattice parameters have been kept to the experimental ones.

The geometry optimization has been realized using a multistep approach. Starting from an intermediate solution of the Rietved refinement, the atomic positions have been relaxed using GGA exchange-correlation potential and considering an FM order. The converged atomic structure has been then optimized using GGA+U with U_{eff} = 2 eV and FM order. Finally, in order to ensure that the long-range magnetic order has negligible effect on the atomic arrangement, the converged

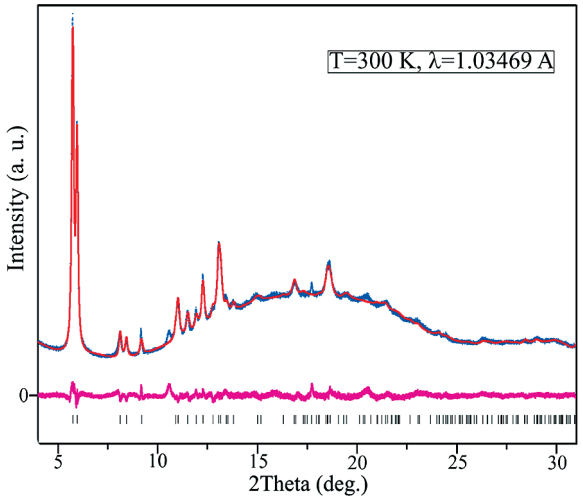

Figure 1. Rietveld output plot of $VO(C_6H_5COO)_2$. Observed (blue) and calculated (red) intensities and their difference curve (pink) are denoted. In addition, calculated Bragg positions of the $VO(C_6H_5COO)_2$ are indicated by vertical ticks.

structure has been relaxed in GGA+U (U_{eff} = 2 eV) based on an AFM order. As expected, no significant structural (bond distances and angles) evolution has been observed between FM and AFM orders, confirming the validity of the FM long-range order to correctly describe the equilibrium atomic arrangement surrounding V^{4+} ions with d^1 electronic configuration and $S = 1/2$ spin state.

The density of states, spin exchange parameters and optical properties are deduced from a self-consistent calculation, using the full-potential linearized augmented plane wave (FP-LAPW) method, as embodied in the WIEN2k code. The maximum l value in the expansion of the basis set inside atomic sphere was 12. The convergence of basis set is controlled by a cutoff parameter $RMT \times K_{max} = 3$, where RMT is the smallest atomic sphere radius in the unit cell and K_{max} is the magnitude of the largest k vector. The self-consistency was carried out on a 8 k-points mesh in the irreducible Brillouin zone, with the following radii RMT(V) = 1.68 au, RMT(O,C) = 1.19 au, RMT(H) = 0.71 au, and GMAX = 20 $Bohr^{-1}$.

Results and Discussion

The chemical analysis of the as synthesized material gave for the chemical composition the following results expressed in atomic percentages: V, 3.85 at %, C, 54.70 at %, H, 20.96 at %. The rest to 100 at % was attributed to the remaining constitutive element oxygen O, 20.49 at %. To further elucidate the chemical composition and vanadium oxidation state, we analyzed the sample by X-ray photoelectron spectroscopy (XPS). Figure S1a in the Supporting Information shows the typical survey spectrum of vanadium oxobenzoate nanofibers. No other core levels related to impurities were detected, proving the high purity of the sample. In general, the difference in binding energies (ΔE) between the O 1s and V $2p_{3/2}$ levels vary for different oxygen content ratios in vanadium oxide compounds. For this reason, the binding energies of vanadium oxide compounds are calibrated typically based on the O 1s peak position.[44] In our case, it was found

(37) Efron, B.; Tibshirani, R. *Stat. Sci.* **1986**, *1*, 54–77.
(38) Kresse, G.; Furthmuller, J. *Phys. Rev. B* **1996**, *54*, 11169–11186.
(39) Blaha, P.; Schwarz, K.; Madsen, G.; Kvasnicka, D.; Luitz, J. WIEN2k, An Augmented Plane Wave + Local Orbitals Program for Calculating Crystal Properties; Technical Universitat Wien: Wien, Austria, 2001; http://www.wien2k.at/.
(40) Perdew, J. P.; Burke, S.; M., E. *Phys. Rev. Lett.* **1996**, *77*, 3865–3868.
(41) Blochl, P. E. *Phys. Rev. B* **1994**, *50*, 17953–17979.
(42) Methfessel, M.; Paxton, A. T. *Phys. Rev. B* **1989**, *40*, 3616–3621.
(43) Monkhorst, H. J.; Pack, J. D. *Phys. Rev. B* **1976**, *13*, 5188–5192.
(44) Silversmit, G.; Delpa, D.; Poelman, H.; Marin, G. B.; Gryse, R. D. *J. Electron Spectrosc. Relat. Phenom.* **2004**, *135*, 167–175.

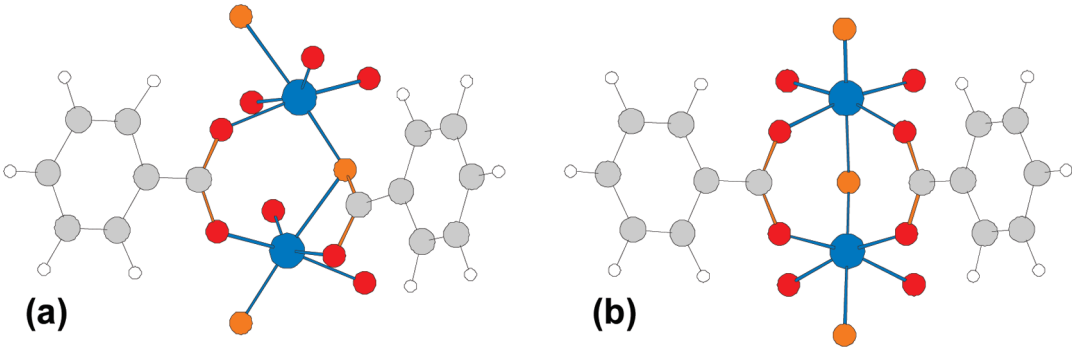

Figure 2. Schematic view of the local arrangement (a) before and (b) after the DFT geometry optimization based on GGA+U (U_{eff} = 2 eV) calculations using an FM order. Vanadium, oxygen, carbon, and hydrogen atoms are respectively represented in blue, red, gray, and white. O3 site is evidenced by an orange color.

from Figure S1b and S1c that the binding energies of O 1s, V $2p_{1/2}$, and V $2p_{3/2}$ levels were 531.8, 524.3, and 517.2 eV, respectively. The peak separation of 14.5 eV (ΔE) between O1s and V$2p_{3/2}$ is close to the energy reported for VO_2, although a small shift in the V$2p_{3/2}$ peak position from 515.6 eV (indexed Hand of X-ray photoelectron spectroscopy) to 517.2 eV was found, from the crystalline VO_2 to the vanadium oxobenzoate nanofibers, respectively. This shift indicates a change of microenvironments for vanadium and confirms that V atoms in vanadium oxobenzoate nanofibers remain in the same formal valence state of V^{4+}.[44] On the basis of the above-mentioned findings, we propose the chemical formula of the as synthesized inorganic−organic hybrid as $VO(C_6H_5COO)_2$ or empirical formula $VO_5C_{14}H_{10}$.

Thermogravimetric analysis (TGA) was performed in order to determine the thermal stability of the vanadium oxobenzoate nanofibers, and to additionally check the suggested chemical formula. From room temperature to 300 °C (Figure S2 in the Supporting Information) only 2.3% of the total weight was lost, indicating a high thermal stability of the vanadium oxobenzoate nanofibers up to this temperature. The weight loss in this range occurs because of the release of physisorbed species like adsorbed water, free OH groups, or some residual organic molecules originating from the employed solvent toluene. The main weight loss of 70.2% as measured relative to the starting point occurs between 300 and 468 °C and is attributed to the decomposition of the organic part of the initial inorganic−organic hybrid. Assuming that the final product of decomposition is the most stable vanadium oxide V_2O_5, the observed net weight loss (70.2%) is consistent with the expected one (70.6%) based on the proposed empirical formula. Accordingly, TGA results corroborate the proposed chemical formula of the investigated inorganic−organic hybrid.

Description of the Structure. Figure 1 shows a typical Rietveld output plot of the synchrotron XRD powder pattern of $VO(C_6H_5COO)_2$ recorded at T = 300 K. An obvious feature is the low crystallinity and/or a high amorphous content (hump in the pattern) originating from the employed synthesis method. A further post-thermal treatment which would certainly increase the crystallinity has not been applied in order to keep the desired inorganic−organic hybrid. Therefore, a relatively low-quality powder pattern has been analyzed with nonstandard methods using rigid body modeling and geometry optimization based on DFT calculations. Careful inspection of the Rietveld plot shows that some peaks (2θ = 9.18, 10.58, 17.74, and 20.48°) are not fully explained by the structural model, which is also reflected in the relatively high value of χ^2 = 4.3. It can be attributed either to impurities of an unknown phase produced as a byproduct during the synthesis, or alternatively, it can be explained at least partly by removing the *C*-centering of the lattice. It would mean that two neighboring VO_6 octahedra in a chain would become independent. We were not able to verify this model, because the resolution of the powder diffraction data was not sufficient (low crystallinity).

Before describing the final structural model, it should be noticed that the geometry optimization was realized based on an intermediate solution of the Rietveld refinement. In particular, the intermediate model was different from the last one by the way that the inorganic and organic blocks were connected to each others. Panels a and b in Figure 2 show the local arrangement around two neighboring V^{4+} ions sites before and after the DFT geometry optimization, respectively, using U_{eff} = 2 eV and FM magnetic order. A significant structure rearrangement was observed. Interestingly, the DFT optimized model exhibits a similar arrangement like the last model deduced from the Rietved refinement.

Such results show the particular stability of the last refined atomic arrangement. The corresponding final crystallographic parameters are summarized in Table 1, refined structural parameters in Table S1 (Supporting Information), geometry optimized structural parameters (U_{eff} = 2 eV) in Table S2 in the Supporting Information, and selected interatomic distances and angles in Table 2. For convenience, the atomic labels from these tables are attached to the corresponding atoms in the scheme given in Figure S3 in the Supporting Information. The asymmetric unit of the vanadium oxobenzoate contains two singly ionized benzoate ligands $C_6H_5COO^-$, and one oxygen anion necessary for V^{4+} charge balance. The metal center is surrounded by six oxygen atoms, four of them from four different $C_6H_5COO^-$ ligands, and two from the remaining structural oxygen which forms two

Table 1. Crystallographic Data and Refinement Parameters Obtained from Synchrotron X-Ray Powder Diffraction

compound name	vanadium oxobenzoate
chemical formula	$VO(C_6H_5COO)_2$
V-oxidation number	+4
space group	*C*2 (No. 5)
mol wt	309.17
Z	4
cryst syst	monoclinic
a (Å)	20.652(3)
b (Å)	6.798(1)
c (Å)	9.954(1)
β (°)	92.145(6)
cell volume (Å^3)	1396.4(9)
calculated density (g/cm^3)	1.470(1)
experimental density (g/cm^3)	1.560(3)
data collection range	4 to 50°
restricted data analysis range	4 to 31°
wavelength (Å)	1.03469(2)
no. of contributing reflns	130
no. of params refined	76
no. of bond lengths restrained	19
no. of bond angles restrained	26
average apparent crystallite size (nm)	28.8
standard deviation of the size, measure of anisotropy (nm)	13.0
R_p (background corr.), R_{wp}, R_{exp}, R_B (%)	16.78, 2.66, 1.28, 1.02
χ^2	4.3

Table 2. Selected Bond Distances and Bond Angles of the Refined Structure and Geometry Optimized Model

atoms	refined model distance (Å)	DFT optimized model distance (Å)	variation (%) $(d_{exp} - d_{DFT})/d_{exp}$
V−O3	1.73(3)	1.699	−1.8
V−O3′	1.87(3)	1.992	6.5
V−O1a	1.925(6)	2.007	4.3
V−O2a	2.008(7)	2.029	1.0
V−O1b	1.971(9)	2.017	2.3
V−O2b	1.996(7)	2.026	1.5
V−V	3.577(9)	3.401	−4.9
O1a−C1a	1.20(2)	1.277	6.4
O1b−C1b	1.49(1)	1.276	−14.4
O2a−C1a	1.49(3)	1.279	−14.1
O2b−C1b	1.50(1)	1.283	−14.5
C1a−C2a	1.49(1)	1.488	−0.1
C1b−C2b	1.30(2)	1.489	14.5
C2a−C3a	1.500(4)	1.405	−6.4
C2b−C3b	1.414(9)	1.402	−0.9
O1a−O2a	2.309(4)	2.270	−1.7
O1b−O2b	2.587(5)	2.271	−12.2
atoms	angle (°)	angle (°)	$(\alpha_{exp} - \alpha_{DFT})/\alpha_{exp}$
O3−V−O3′	144.2(1)	177.3	22.9
O1b−V−O2b	138.9(3)	172.5	24.2
O1a−V−O2a	147.6(2)	169.8	15.0
O1a−V-O2b	81.1(3)	88.1	8.7
O2a−V-O1b	89.7(3)	90.1	0.5
O3−V−O1b	84.3(5)	92.7	10.0
O3−V−O1a	79.2(4)	96.3	21.6
O3′−V−O1b	74.8(3)	84.9	13.4
O3′−V−O1a	66.9(4)	85.0	27.0
V−O3−V	167.6(1)	134.1	−20.0
O1a−C1a−O2a	117.0(9)	125.2	7.0
O1b−C1b−O2b	119.2(5)	125.1	5.0
C3a−C2a−C7a	114.4(7)	119.8	4.7
C3b−C2b−C7b	116.8(9)	119.7	2.5

short bonds with the lengths of 1.73(3) and 1.87(3) Å in the Rietveld model, whereas only one bond is short (vanadyl bond) in the DFT model. The resulting coordination polyhedron around each vanadium atom, in the Rietveld model, is a distorted octahedron with V−O bond lengths (Table 2) in the range 1.73(3)−2.008(7) Å. The O−V−O bond angles lie in the range 66.9(4)−147.6(2)°, which appreciably deviate from the values for regular octahedron of 90 and 180°. For comparison, a geometry-optimized solution presented in the third column of Table 2 exhibits less-distorted VO_6 octahedron, i.e., O−V−O bond angles are quite close to 90 or 180°.

Although the DFT and Rietveld models are similar from the architectural point of view, important structural differences are observed in terms of bond lengths and angles. A close inspection of the structural variations between the last Rietveld model and the DFT optimized structure leads to the following observations.

For the V−O bond lengths, an increase of 2.4% from 1.916 to 1.962 Å is observed between the Rietveld and the DFT models, with distances ranges of [1.731−2.007] and [1.699−2.029] Å, respectively. In particular, the double bond character of the vanadyl bond is enhanced in the DFT model (contraction of about 2%). For the C1−O bond lengths, a decrease of about 10.3% from 1.426 to 1.278 Å is observed between Rietveld and DFT models, with distances ranges of [1.202−1.500] and [1.275−1.282] Å, respectively. It should be noticed that the standard deviation is significantly reduced after the geometry optimization, from 0.149 to 0.003 Å. Additionally, the average C1−O distance in the DFT model is 1.278 Å, which is in between the values expected for a double bond, 1.24 Å, and a partial double bond, 1.36 Å. For the C1−C bond lengths, a decrease of about 0.4% from 1.494 to 1.488 Å is observed between Rietveld and DFT models, confirming its single-bond character (expected values ranging from 1.49 to 1.54 Å). For the others C−C bond lengths, which are involved in the ring, an increase of 0.6% from 1.389 to 1.398 Å is observed between the Rietveld and DFT models, with distances ranges of [1.200−1.500] and [1.391−1.404] Å, respectively. As for the C1−O distances, a significant decrease in the standard deviation is observed from 0.109 to 0.005 Å. These distances in between 1.39 and 1.40 Å in the DFT model agree quite well with the expected value for C−C bond lengths involved in an aromatic ring (1.39 Å). Finally, it should be noticed that a very short O−O contact was obtained in the Rietveld model between O3 and O1b atoms of 2.116 Å. After the geometry optimization, this contact has been increased to 2.751 Å, i.e., an increase of 30% of the distance.

In summary, the DFT structural model is more regular than the Rietveld one, both in terms of bond lengths and angles. Different arguments could be given to explain such a difference: (1) a theoretical treatment at 0 K appears to be inadequate to correctly describe the room-temperature structure, (2) a too short coherence length leading to strong uncertainties in the Rietveld refinement. As a matter of fact, one way to resolve this dilemma is to estimate the oxidation state of the V^{4+} ions in the structure by calculating the well-known bond-valence sum rule.[45] Calculating the bond-valence sum

(45) Brown, I. D.; Kang Kun, W. *Acta Crystallogr., Sect. B* **1976**, *32*, 1957–1959.

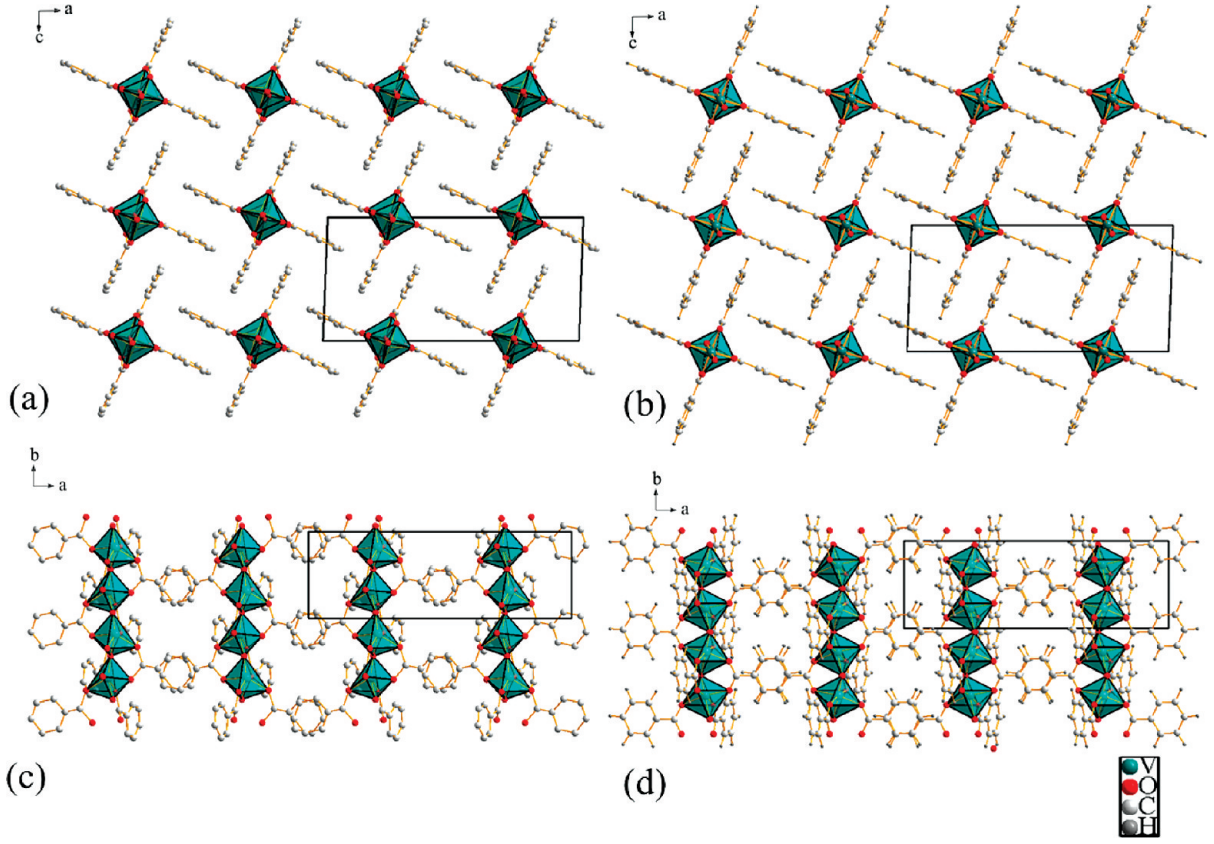

Figure 3. Solved and refined final crystal structure of $VO(C_6H_5COO)_2$ viewed (a) along the *b*-axis, and (c) along the *c*-axis. A geometry optimized crystal structure of $VO(C_6H_5COO)_2$ based on DFT calculation is displayed in (b) along the *b*-axis, and in (d) along the *c*-axis. Projection of the unit cell is indicated by solid lines.

(BVS) for vanadium atom in the VO_6 coordination octahedron, one obtains the value of BVS of 4.35 for the refined model and 3.94 for the calculated one. Because the oxidation state of vanadium is deduced being +4, both BVS values agree well with it, confirming the validity of the proposed structural model for $VO(C_6H_5COO)_2$. However, a better agreement is obtained with the DFT model confirming the necessity to properly describe both the vanadyl bond and the more regular geometry of the octahedron around V^{4+} ions. In other words, although the DFT arrangement is more regular than the Rietveld one, it also leads to a strong V−O bond alternation. The present analysis leads to the conclusion that the discrepancy between the Rietveld and DFT models is mainly due to the low crystallinity of the investigated material, leading to strong uncertainties. However, if the XRD pattern exhibits the features typical of a low crystalline product and the initial structure of the DFT geometry optimization was far from the final solution, both techniques converged independently toward the same architecture. Such results clearly illustrate the interest to support XRD analysis by DFT relaxation in the case of poorly crystallized samples.

Concerning structure description, two crystallographically independent benzoate ligands act in the same fashion. Both the COO^- groups of singly ionized benzoate moieties link adjacent metal centers forming infinite parallel chains along the 2-fold symmetry *b*-axis, which is nicely illustrated in Figure 3. The major difference between these two independent ligands is in their planar conformation, because they lie in almost mutually perpendicular planes whose normal vectors are both perpendicular to the *b*-axis (panels a and b in Figure 3). The resulting structure consists of chains of corner-shared VO_6 octahedra (mutually linked with the oxygen atom O3) running along the *b*-axis with a V−V separation of about 3.6 Å (c and d in Figure 3). In terms of connectivity along the *b*-axis, the structure can be regarded as a staggered V−V−V chain, where adjacent chains, separated from each others by the organic part composed of benzoate moieties, are mutually distant by 9.95 Å and 9.855 Å, respectively, along the *c*- and *a*-axes.

The second parameter that might serve as a criterion to validate the structural model is the experimentally determined bulk density of the compound. Comparison of the experimentally determined density of $\rho = 1.560(3)$ g/cm^3 with the corresponding calculated X-ray density $\rho_{calcd} = 1.470(1)$ g/cm^3 shows a slight discrepancy that might be attributed to the presence of unidentified impurities and a considerable amount of an amorphous content in the analyzed material.

Finally, let us briefly discuss the microstructural properties of the investigated vanadium oxobenzoate nanofibers. It is generally expected in a system of reduced dimensionality that anisotropic broadening occurs, i.e., crystallite sizes might show a strong anisotropic charac-

ter.[27] As already mentioned in the experimental part, the anisotropic size broadening is considered in general to be a phenomenological model, in which using the Scherrer formula it can be written as a linear combination of spherical harmonics.[46] After refinement of the expansion coefficients, the Rietveld program calculates the crystallite size along each reciprocal lattice vector. The resulting extracted apparent crystallite size for each reflection *hkl* is displayed in Figure S4 in the Supporting Information as a function of 2θ in the selected range from 5 to 21°. It is noteworthy that the difference between minimum and maximum value of the size is quite high, i.e., 13 and 75 nm. The highest value of the crystallite size (75 nm) corresponds to the 020 reflection (direction of the *b*-axis), which is most probably the preferred growth direction of the nanofibers. This feature is in accordance with the proposed structural model of parallel one-dimensional chains arranged along the crystal *b*-axis (Figure 3). Such structural arrangement remains aligned in the final morphology, thus forming nanofibers with the long axis parallel to the crystal *b*-axis.

The microstructural properties of the final product, including morphology and local crystallinity, have been probed by electron microscopy including TEM, electron diffraction, and SEM. A representative SEM overview image of $VO(C_6H_5COO)_2$ is displayed in Figure 4a, from which it seems that the entire material is rather homogeneous consisting of long nanofibers up to 10 μm in length and even up to 100 nm in diameter. However, a higher-magnification SEM image, in Figure 4b, clearly discloses that the nanofibers are not so uniform, but some of them exhibit a complex morphology consisting of mutually aligned individual nanofibers as can be particularly seen in the upper left corner of Figure 4b. A typical TEM image (inset in Figure 4b) reveals the presence of individual nanofibers having a distribution of their widths with a mean value of 41 nm, and a standard deviation of 10 nm. Figure 4c shows a magnified TEM image of two isolated nanofibers, where variation of the contrast along the axes of the nanofiber confirms their complex morphology. The well-resolved individual parts, i.e., parallel aligned nanofibers, are clearly visible corroborating the SEM findings. The local crystallinity of the individual nanofiber has been tested by recording the corresponding electron diffraction pattern, taken from a selected region of a single nanofiber. The resulting pattern is displayed in Figure 4d, showing that it consists of discrete Laue spots, thus revealing the single-crystallinity of the part of the investigated individual nanofiber. In addition, the symmetry of the Laue spots and the corresponding reflection assignment make it possible to identify the zone-axis as [001] (*c*-axis), which is in this case parallel to the thickness of the nanofiber. Similarly, the long axis of the nanofiber or the growth direction is identified as [020] (*b*-axis), whereas the width of the nanofiber is then along [200] (*a*-axis). In this way, the TEM results nicely confirm the anisotropic crystallite

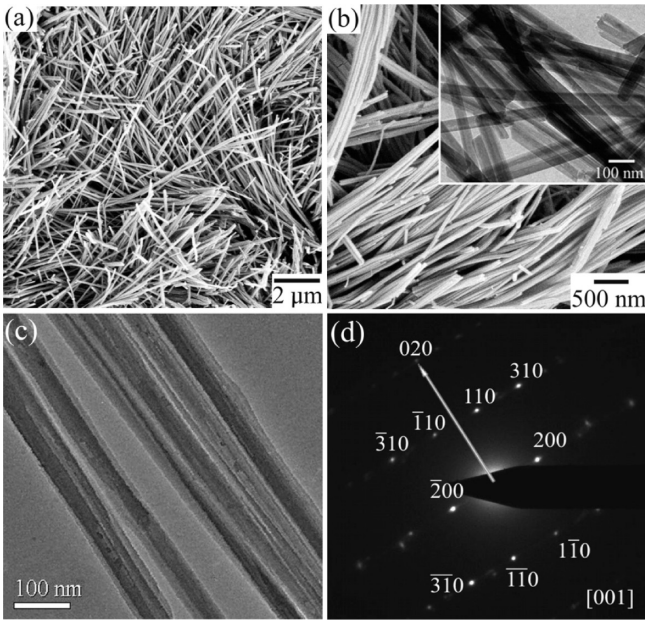

Figure 4. (a) Overview SEM image of the as-synthesized vanadium oxobenzoate nanofibers. (b) SEM image recorded at a higher magnification. In the inset TEM image of individual nanofibers is shown. (c) Higher-magnification TEM image of several parallel aligned nanofibers. (d) Indexed SAED pattern of the single nanofiber in [001] zone-axis, and growth direction [020] is denoted by the arrow.

sizes as deduced from XRD analysis. On the other hand, one can notice that the length of the nanofibers is up to ten micrometers, but the apparent size along the *b*-axis is only 75 nm. This observation implies that the structural coherency is not kept along the whole length of the nanofiber. It is then reasonable to conclude that the powder is constituted of polycrystalline $VO(C_6H_5COO)_2$ nanofibers, themselves based on the assembly of smaller single-crystalline units. Unfortunately, the present compound is highly sensitive to the e-beam, because of the high content of organics, and therefore detailed HRTEM analysis is not possible. Any HRTEM imaging yields to amorphous-like data without resolvable crystal lattice fringes.

The nature of the amorphous by product was investigated by local probe technique like TEM-EDX and by visual analysis of TEM/SEM images. From SEM as well as TEM images, no separate amorphous phase was observed, since the material displayed therein looks rather homogeneous. Moreover, thorough washing of the final material with ethanol certainly removed most of the excess of purely organic byproducts, leaving behind the targeted inorganic−organic hybrid compound.

To get more insight about the organic moieties and their binding to the metal centers, the investigated compound has been probed by FT-IR spectroscopy. The resulting spectrum, which is displayed in Figure 5, consists of a bunch of absorption peaks reflecting a high structural complexity of this inorganic−organic hybrid compound.

The spectrum can be divided in two parts: Characteristic bands corresponding to the different molecular vibrations of the benzoate ligand, and the bands attributed to vibrations of the inorganic O−V−O octahedral

(46) Jarvinen, M. *J. Appl. Crystallogr.* **1993**, *26*, 525–531.

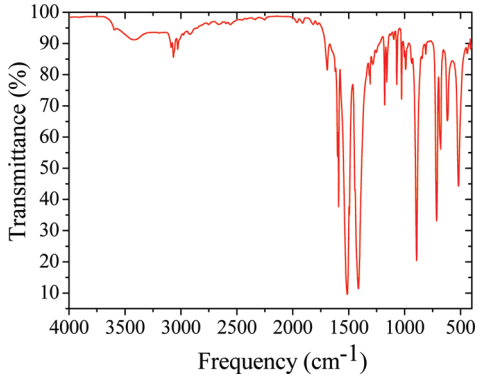

Figure 5. FT-IR spectrum of $VO(C_6H_5COO)_2$.

framework. The broadband centered at 3417 cm^{-1} is attributed to O−H stretching modes of the hydroxyl groups of adsorbed water molecules and hydrogen-bonded OH groups. Moreover, the presence of the sharp absorption band centered at 3593 cm^{-1} is normally assigned to the stretching of free hydroxyl groups, again most probably attached on the surface of the nanofibers. It is interesting to note that the bands at 927 and 1287 cm^{-1}, characteristic of the dimeric structure of benzoic acid, are still observed, pointing to the fact that a small amount of benzoic acid dimers are also present in the sample. The bands at 1599, 1511, and 1493 cm^{-1} are characteristic of the skeletal vibrations of the phenyl ring, the bands at 3028 and 3066 cm^{-1} can be assigned to C−H stretching of the phenyl ring, and the band at 1179 cm^{-1} with the tail at 1162 cm^{-1} is typical of C−C vibration.[25,47,48] In the low-frequency range of 811−700 cm^{-1}, another set of characteristic frequencies of the phenyl ring are observed, specifically the band at 714 cm^{-1} corresponding to the C−H out of plane deformation and the one at 677 cm^{-1} related to the C=C deformation.[48] Important information about the binding of the organic moieties, the benzoate anions, or more precisely the carboxylate groups COO^-, to the metal centers can be deduced by comparing the difference of frequencies between its antisymmetric ν_a and symmetric ν_s stretching modes. The carboxylate anion may coordinate to metals in three modes: monodentate, bidentate chelating (bonded to one V) and bidentate bridging (bound to two V), where each mode has its own stretching vibration frequency that allows us to distinguish them.[49] In the IR spectrum, $\nu_a(COO^-)$ is located at 1590 cm^{-1} and $\nu_s(COO^-)$ at 1413 cm^{-1}, leading to a difference of Δ = 177 cm^{-1}. Monodentate coordination leads to a significantly higher difference between asymmetric and symmetric carboxylate frequencies in the range 380−450 cm^{-1}. Therefore such a coordination can be certainly excluded.[25,50] On the basis of the IR results, discrimination between bidentate bridging and bidentate chelating coordination is not so straightforward. However, it is usually reported that bidentate chelating appears with much smaller frequency differences between 40 and 70 cm^{-1},[25] guiding us to conclude that the most probable coordination of the carboxylate group to the vanadium centers is bidentate bridging, where two subsequent vanadium cations are coordinated to one carboxylate group as already deduced from XRD and DFT geometry optimization. Consequently, FT-IR results nicely support the suggested structure of vanadium oxobenzoate.

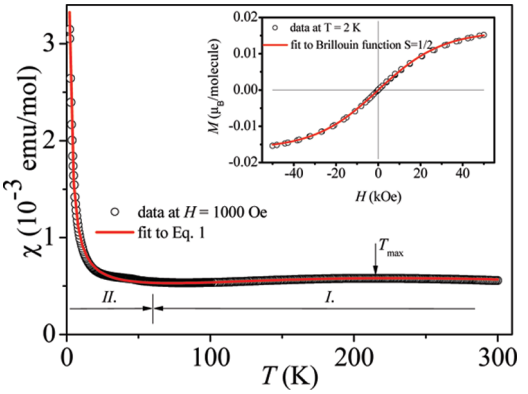

Figure 6. Temperature-dependent susceptibility of the vanadium oxobenzoate and fit to eq 1. In the inset, we show the magnetization as a function of the magnetic field at 2 K and fit with the Brillouin function.

To explore the magnetic properties of the new vanadium oxobenzoate, we performed DC magnetization and EPR measurements. According to the $VO(C_6H_5COO)_2$ atomic structure, only V^{4+} ions, with spin quantum number $S = 1/2$, are expected to carry a nonzero magnetic moment. As they are arranged in chains the magnetic properties characteristic for one-dimensional systems[33] and possible instabilities, such as spin-Peierls transition, at low temperature were expected to be detected.[51]

The temperature dependence of the susceptibility displayed in Figure 6 can be divided into two regions. (I) In the high-temperature region, between 300 and 60 K, the susceptibility, χ, shows a broad maximum at around $T_{max} = 215$ K, indicating AFM interactions between V^{4+} moments along the V−V−V chains. The broad maximum in χ is very typical for 1D AFM systems and has been for instance observed in Cu^{2+} chains.[52,53] Unusually, high T_{max} value marks very strong superexchange interactions between V^{4+} ($S = 1/2$) moments. (II) In the low-temperature region, i.e., for $T < 60$ K, a small "bump" in the susceptibility is noticed around 50 K. However, this anomaly has not been seen in all batches, so we believe that it is not of intrinsic origin. Below 40 K, the susceptibility starts to increase again, showing a typical Curie-like tail. To investigate the nature of paramagnetic moments that cause the Curie-like tail, we measured the magnetization versus magnetic field at 2 K. The inset to Figure 6 shows a characteristic paramagnetic S-shaped

(47) Tocchetto, A.; Glisenti, A. *Langmuir* **2000**, *16*, 6173–6182.
(48) Caravati, M.; Grunwaldt, J.-D.; Baiker, A. *Phys. Chem. Chem. Phys.* **2005**, *7*, 278–285.
(49) Zhu, Y.; Li, H.; Y., K.; Gedanken, A. *J. Mater. Chem.* **2002**, *12*, 729–733.
(50) Doeuff, S.; Henry, M.; Sanchez, C.; Babonneau, F. *J. Non-Cryst. Solids* **1987**, *89*, 206–216.
(51) Peierls, R. E. Quantum Theory of Solids; Oxford University Press: London, 1955.
(52) Mastropietro, T. F.; Armantano, D.; Grisolia, E.; Zanchini, C.; Lloret, F.; Julve, M.; De Munno, G. *Dalton Trans.* **2008**, 514–520.
(53) Lee, Y. M.; Lee, H. W.; Kim, Y. I. *Polyhedron* **2005**, *24*, 377–382.

magnetization curve without detectable hysteresis. As a matter of fact, the measured data can be fitted with the Brillouin function for $S = 1/2$ spins, which is the value expected for V^{4+} ions. So we explain this paramagnetic signal at low temperature as a contribution of noninteracting V^{4+} ions that are not perfectly incorporated in the AFM ordered chains.

The main feature in the $\chi(T)$ data describing our system corresponds to the high-temperature region I), where the susceptibility shows a maximum value approximately at 215 K. After correction for the magnetic susceptibility for the diamagnetic contribution we tried to reproduce the experimental data with a rationale function[54] that simulates the Boner−Fisher curve[55] describing the susceptibility of a linear magnetic chain with the isotropic interaction between nearest neighbors: $H = -2J \Sigma S_i \cdot S_j$. We add a Curie term for spin $S = 1/2$ to the function[54] to account for the noncoupled magnetic moments and obtain

$$\chi = (1-\rho)\frac{N_A g^2 {\mu_B}^2}{k_B T}\frac{0.25+0.14995x+0.30094x^2}{1.0+1.9862x+0.68854x^2+6.0626x^3} + \rho\frac{N_A g^2 {\mu_B}^2}{4k_B T} \quad (1)$$

where ρ is the molar fraction of noncoupled moments, N_A the Avogadro number, $g = 1.96$ obtained from EPR measurements (see below), μ_B the Bohr magneton, k_B the Boltzmann constant and finally $x = |J|/T$ where the magnetic spin exchange interaction J (in Kelvins) is negative for AFM coupled magnetic moments. The best fit of function 1 to the experimental data (full line in Figure 6) was obtained with $J = -189$ K and $\rho = 0.004 = 0.4\%$ noncoupled V^{4+} magnetic moments. The value of ρ corresponds to about one unpaired V^{4+} ion per 250 V^{4+} ions incorporated into the perfect chains. The average length of the unperturbed chains is then $l = 250 \times 0.35$ nm $= 87$ nm, which is almost identical to the crystallite size along the *b*-axis. Because the V-chains grow along this axis, the detected Curie contribution in fact corresponds to the surface V^{4+} sites.

In addition, X-band EPR measurements were performed in order to investigate the ground state of vanadium oxobenzoate. A typical X-band EPR spectrum measured at room temperature is shown in the inset of Figure 7a. The EPR line shape cannot be simply described with a single Lorentzian. Two overlapping Lorentzian components are needed to perfectly reproduce the measured X-band EPR line shape. However, the parameters for the two components are rather similar and show very similar temperature dependence suggesting that both components arise from the same region of the sample. For this reason, we proceed with a moment analysis: the first moment defines the center of the line and therefore the *g*-factor, whereas the square root of the second moment gives the full-width at half-maximum line width $\sqrt{M_2} = \Delta H_{fwhm}$. The calibrated intensity of the room temperature EPR signal roughly corresponds to the total EPR susceptibility measured by SQUID (Figure 6). The room-temperature EPR line width is $\Delta H_{fwhm} = 270$ G, whereas the *g*-factor is 1.962(2). We note that the *g*-factor is rather characteristic of V^{4+} centers in an octahedral environment. The observed structural distortion of the VO_6 octahedra (Figure 2) should lead to an axially symmetric *g*-factor with $g_x = g_y = g_e - 2(\lambda/\delta)$ and $g_z = g_e - 8(\lambda/\Delta)$.[56] Here $\lambda = 170$ cm^{-1} is the spin orbit coupling constant of V^{4+}. Although we are not able to reliably determine g_x, g_x, and g_z from the present powder X-band EPR data, we can estimate the crystal field parameters $\delta = 2100$ cm^{-1} and $\Delta = 8400$ cm^{-1}. On cooling from 400 K to ~230 K, the integrated EPR susceptibility χ_{EPR} increases with decreasing temperature (Figure 7a), similarly as found in the magnetic susceptibility measurements (Figure 6). Below T_{max}, χ_{EPR} starts to decrease reaching a minimum at $T_{min} = 28$ K. However, the observed χ_{EPR} does not imply opening of a spin gap that would be characteristic of 1D magnetic instabilities. In the entire temperature interval, between 400 K and T_{min}, the line shape remains almost unchanged. Below T_{min}, the line shape qualitatively changes and the EPR signal intensity starts to increase again. The line shape changes are however subtle and further high-field EPR experiments are needed to understand the evolution of the EPR below T_{min}. The temperature dependence of χ_{EPR} is therefore indicative of the one-dimensional character of V^{4+} Heisenberg exchange interactions at least between 400 K and T_{min}. It is not clear however if the increase in χ_{EPR} is due to the impurity signal with a Curie-like

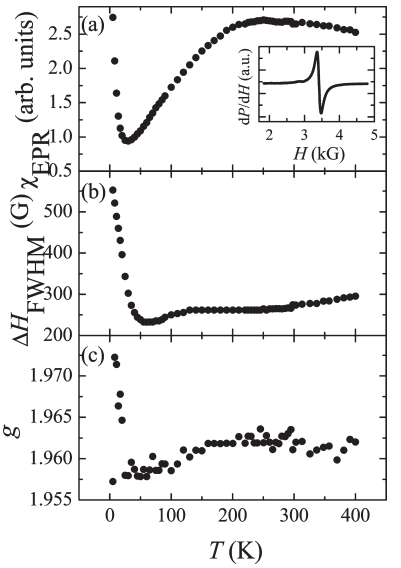

Figure 7. Temperature dependence of X-band EPR parameters for the vanadium oxobenzoate: (a) dependence of the integrated EPR spin susceptibility, (b) full-width at half-maximum line width, and (c) *g*-factor. In the inset to (a), we show a typical room-temperature X-band EPR spectrum.

(54) Estes, W. E.; Gavel, D. P.; Hatfield, W. E.; Hodgson, D. J. *Inorg. Chem.* **1978**, *17*, 1415–1421.
(55) Bonner, J. C.; Fisher, M. E. *Phys. Rev.* **1964**, *135*, A640–A658.
(56) Abragam, A.; Bleaney, B. Electron Paramagnetic Resonance of Transition Ions. Clarendon Press: Oxford, U.K., 1970.

dependence or due to some short-range ordering of the V^{4+} moment in the VO_6 chains.

Further insight into the magnetic behavior of vanadium oxobenzoate is obtained from a close inspection of the temperature dependence of ΔH_{fwhm}. Within the high-temperature Kubo−Tomita expansion, which predicts the exchange-narrowed line width to be $\Delta H_{fwhm} \approx (2/(g\mu_B))(M_2/|J|)$, we estimate that a magnitude of the magnetic anisotropy, which is responsible for the second moment M_2, is about 3.5 K. This value is at least an order of magnitude larger than it would be expected to be for the dipolar contribution. Therefore, we suggest that large M_2 could be explained by considering Dzyaloshinski−Moriya interaction, which is in our case allowed by the crystal symmetry. At high-temperatures an almost linear dependence of ΔH_{fwhm} has been noticed (Figure 7b). When T decreases and approaches $\sim T_{max}/2$, the slope of ΔH_{fwhm} starts to change. Below 50 K, ΔH_{fwhm} starts to dramatically increase with decreasing temperature and reaches more than 500 G at 4 K. In the same temperature interval, the g-factor, which was temperature-independent at high-temperatures, also increases monotonically, reaching 1.975(3) at 4 K (Figure 7c). Two scenarios could explain the low-temperature changes in EPR: (i) As we have already mentioned above, the presence of surface V^{4+} sites is significant and the low-temperature EPR line shape may be ascribed to these centers. Due to the coupling of the surface V^{4+} centers to the bulk V^{4+} moments in the chains, we propose that the residual temperature dependence of the line width may then reflect the slowing down of the chain spin dynamics in the low-temperature regime. (ii) Alternatively, the observed changes in EPR may indicate a crossover to the predicted quantum one described by the Oshikawa−Affleck (OA) theory for one-dimensional quantum spin Heisenberg chains with the staggered field.[57,58] The origin of the staggered field may be in our case either the Dzyaloshinski−Moriya interaction, already announced by the high-temperature dependence of the line width, or the g-factor variation due to the tilting of VO_6 octahedra along the chain. Additional high-field frequency-dependent EPR measurements are needed to discriminate between these two possibilities.

Let us sum up the experimental results. A new compound has been obtained with the chemical formula $VO(C_6H_5COO)_2$. The final product of the synthesis is a yellow-green powder indicating that the material partially absorbs the visible light. Such macroscopic observation is the signature of the presence of two absorption bands, respectively centered at about 2 and 3 eV. Additionally, from the color of the powder, we can conclude that $VO(C_6H_5COO)_2$ is a semiconducting compound. Magnetic data of $VO(C_6H_5COO)_2$ have been interpreted as originating from a spin-half AFM chain system with an estimated spin exchange parameter $J = -189$ K.

(57) Oshikawa, M.; Affleck, I. *Phys. Rev. Lett.* **1999**, *82*, 5136–5139.
(58) Oshikawa, M.; Affleck, I. *Phys. Rev. B* **2002**, *65*, 134410.

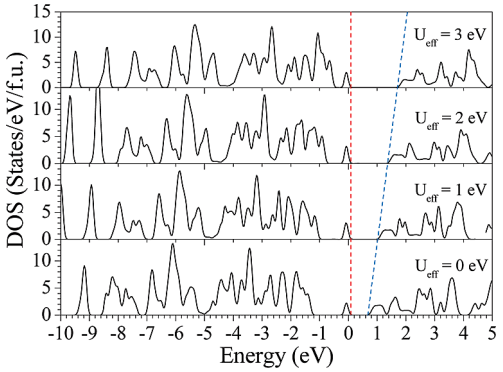

Figure 8. Total densities of states (up-spin) of the DFT optimized vanadium oxobenzoate with the AFM order and for different U_{eff} parameters. The Fermi level is set to 0 eV; the top of the valence band as well as the bottom of the conduction band are denoted with the red (blue) dashed lines, respectively.

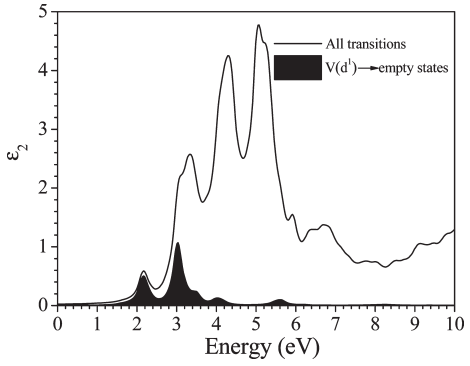

Figure 9. Prediction of the imaginary part of the dielectric function as a function of the incident photon energy (solid line), based on GGA+U (U_{eff} = 2 eV) calculations. The optical transitions starting from the $V(d^1)$ level are represented in black.

To corroborate these experimental results and interpretations, we have estimated the optical and magnetic properties of the optimized structure based on DFT calculations. Before discussing these results, we first consider the effect of the U_{eff} parameter on the electronic structure. Up-spin total densities of states (DOS) related to the optimized DFT model with different U_{eff} values are represented in Figure 8. These calculations have been carried out on the basis of the AFM magnetic structure (up and down spin total DOS's are then equivalent). The general features of these DOS's are similar except for a significant change in the V(d) bands positions as a function of the U_{eff} value. Particularly, it leads to a band gap increase from 0.7 to 1.7 eV when U_{eff} is raised from 0 to 3 eV. To better understand the consequence of the band gap increase on the optical properties and to properly relate the yellow-green color of the powder to the so-obtained DOS's, we have realized calculation of the dielectric function. Figure 9 shows the imaginary part of the dielectric function for a U_{eff} value of 2 eV, leading to a good agreement with the experimental observations. In fact, if the band gap in the DOS is only 1.7 eV, the resulting absorption spectrum leads to two absorption bands, respectively centered at 2.2 and 3 eV. The combination of an intense absorption band at 3 eV and a less intense absorption at 2.2 eV allows us to explain the

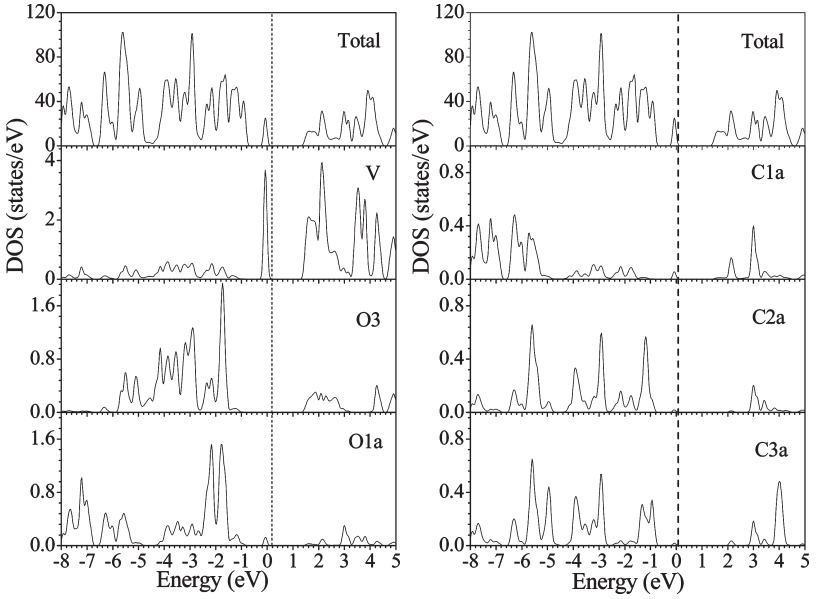

Figure 10. Partial densities of states of $VO(C_6H_5COO)_2$ in the AFM order. The Fermi level is set to 0 eV.

yellow color (due to the presence of the 3 eV band) of the powder with some greenish aspects (due to the simultaneous presence of the two bands).

To have more insights about the origin of these two bands, we could first have a look at the partial DOS (pDOS) for $U_{eff} = 2$ eV. Figure 10 shows the sum of spin-up and spin-down DOS's projected on selected sites.

Below the Fermi level, the occupied bands could be described as based on two main blocks. The first part from −8 to −1 eV is mainly composed of C(2p) states and O(2p) states interacting with V(3d) states. In the present case, the VO_6 octahedron is distorted with shorter bonds along the *z*-axis of the octahedron, meaning that the first V(3d) orbital will be $3d_{xy}$, followed by the two nearly degenerate orbitals $3d_{xz}$ and $3d_{yz}$, then $3d_{x^2-y^2}$ and finally the highest orbital $3d_{z^2}$. The second part, just below the Fermi level, is mainly based on V($3d_{xy}$) states interacting with O(2p) states. As a consequence, the present DOS's confirm the d^1 electronic configuration of vanadium atoms and its 4+ formal oxidation state. It should be noticed that no interaction between V(3d) orbitals and O3 (2p) orbitals are observed, while a significant contribution of O1a, O2a, O1b, and O2b is observed (as illustrated in Figure 10 with O1a pDOS). Such observation could be easily explained on the basis of geometrical arguments. As expected, the $3d_{xy}$ orbital does not interact with the bridging apical oxygen ligand (O3) for symmetry reasons. In contrast, this orbital, which comes from the t_{2g} block of the regular octahedron, could interact with the basal plane oxygen atoms (O1a, O1b, O2a, and O2b). This observation has a strong impact allowing to understand the magnetic spin exchange path in such a system. The superexchange path V($3d_{xy}$) − O3(2p) − V($3d_{xy}$) will have a negligible effect, while the supersuper-exchange path V($3d_{xy}$) − O1a(2p) − O1b(2p) − V-($3d_{xy}$) will be significant. It should also be noticed that some of the C(2p) orbitals of the benzoate molecules contribute in the magnetically active orbital V($3d_{xy}$), demonstrating the strong interaction and delocalization between the atomic orbitals of these ligands. In other words, the magnetic moment in such a system will be signifi-

cantly delocalized over the whole benzoate molecule. Above the Fermi level, the first empty states are mainly based on V($3d_{xz}$, $3d_{yz}$) orbitals interacting with O3(2p) orbitals.

As a consequence, from the present analysis the first optical transition will be from the V($3d_{xy}$) band to the V ($3d_{xz}$, $3d_{yz}$) bands. All the optical transitions starting from the V($3d_{xy}$) level are represented in black in Figure 9, confirming the nature of the first optical transitions in VO-$(C_6H_5COO)_2$.

Finally, the present DFT calculations may also be used to estimate the magnetic spin exchange parameters in VO $(C_6H_5COO)_2$. As we just emphasized from the analysis of the orbital overlap, the main magnetic paths are super-super-exchange $V3d_{xy}$ − O1a(2p) − O1b(2p) − $V3d_{xy}$ and $V3d_{xy}$ − O2a(2p) − O2b(2p) − $V3d_{xy}$. Both structural and magnetic data lead to argue that $VO(C_6H_5COO)_2$ at low temperature is a 1D antiferromagnetic system, with one magnetic spin exchange parameter, J_{intra}, corresponding to the intrachain supersuper-exchange interaction. The interchain interaction, J_{inter}, is expected to be negligible particularly if we consider that V−V separation along *a* and *c* are larger than 9.5 Å.

To estimate the strength of these *J* values and confirm the present 1D picture, we have considered three magnetic ordered structures . The first model, denoted FM, is only based on ferromagnetic (FM) interactions. The second model, AFM1, is based on AFM interactions along the chain and FM interactions between the chains. The third model, AFM2, is based on AFM interactions along the chain and between the chains. As expected, AFM1 and AFM2 orders are more stable than the FM model. In addition, the energy difference between AFM1

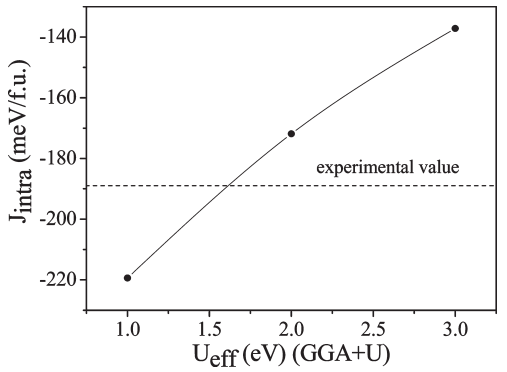

Figure 11. Intrachain magnetic spin exchange of $VO(C_6H_5COO)_2$ as a function of U_{eff} value, deduced from GGA+U DFT calculations.

and FM is the same than between AFM2 and FM (−29.6 meV/f.u.), meaning that the interchain spin exchange interaction is not significant. The energies of these three ordered spin states can be evaluated using the Heisenberg spin Hamiltonian written in terms of the two spin exchange parameters, J_{intra} and J_{inter}.

$$E(\mathrm{FM}) = -J_{intra} - J_{inter} \quad (2)$$

$$E(\mathrm{AFM1}) = +J_{intra} - J_{inter} \quad (3)$$

$$E(\mathrm{AFM1}) = +J_{intra} + J_{inter} \quad (4)$$

By mapping the energy differences between the ordered spin states given by the spin Hamiltonian (relations 2, 3, and 4) onto those given by the GGA+U calculations, we obtain J_{intra} and J_{inter} values. For $U_{eff} = 2$ eV, $J_{intra} = -171.9$ K and $J_{inter} = -0.2$ K, meaning that only intrachain interactions are relevant to describe the magnetic properties of $VO(C_6H_5COO)_2$. Figure 11 shows the evolution of the J_{intra} spin exchange value as a function of the U_{eff} parameter. As for the optical properties, the choice of $U_{eff} = 2$ eV leads to reasonable results in comparison to the experimental estimation of $J = -189$ K.

The present decrease in the spin exchange strength with increasing U_{eff} parameter is directly related to the increase of the band gap with U_{eff}. In fact, increasing U_{eff} value leads to a relocalization of the V(3d) orbitals. As a consequence, the V(3d) − O(2p) interaction is reduced and the supersuper-exchange path is less efficient. These last DFT results, in regards with the magnetic data, confirm the highly anisotropic nature of the magnetic interaction in $VO(C_6H_5COO)_2$ and the 1D character based on a dominant supersuper-exchange intrachain interaction. Considering the AFM1 magnetic structure, the magnetic moment of vanadium has been estimated to be about 0.73 μ_B. It should be noticed that this value appeared to be not sensitive to the U_{eff} parameter for values up to $U_{eff} = 3$ eV.

Conclusions

We have synthesized a new compound within the group of nanocrystalline inorganic−organic hybrids, vanadium oxobenzoate $VO(C_6H_5COO)_2$, using a simple solvothermal reaction between vanadium(V) oxytriisopropoxide and benzoic acid in toluene. The crystal structure of this compound has been solved from the synchrotron X-ray powder diffraction pattern in an unconventional way by combining a direct space method, DFT geometry optimization, and in the last step, a constraint Rietveld refinement. Such a combination of complementary approaches was crucial for the successful crystal structure determination of such a material with low crystallinity, for which conventional approaches failed to solve the structure. The compound crystallizes in the monoclinic crystal system, in the *C*2 space group with the following lattice parameters: $a = 20.652(3)$, $b = 6.798(1)$, $c = 9.954(1)$ Å, $\beta = 92.145(6)°$. The inorganic part of the structure can be regarded as staggered V−V−V chains, formed of corner-sharing VO_6 octahedra, running along the monoclinic *b*-axis, with a V−V separation of about 3.6 Å. In addition, it should be noticed that a strong V−O bond alternation is suggested by the present DFT calculations. The organic part is based on two crystallographically independent singly ionized benzoate moieties, linked to vanadium atoms through a bidentate bridging mode, where two subsequent vanadium cations are coordinated to one carboxylate group. The morphology of $VO(C_6H_5COO)_2$ is rather complex, exhibiting several micrometers long nanofibers, and each nanofiber consists of smaller subunits aligned in parallel to the growth direction along the *b*-axis as expected form the 1D nature of the compound. The magnetic susceptibility and X-band EPR measurements shows that the magnetic properties of $VO(C_6H_5COO)_2$ can be described by a $S = 1/2$ linear antiferromagnetic chain model with the isotropic interaction between nearest neighbors and an estimated magnetic spin exchange parameter of $J = -189$ K. EPR measurement further confirms the structural model, since EPR determined *g*-factor equals to 1.962 (2), which is rather characteristic of V^{4+} centers in an distorted octahedral environment. The present experimental picture of $VO(C_6H_5COO)_2$ was supported by DFT calculations, using GGA+U method with $U_{eff} = 2$ eV, at least. In particular, the simulated optical response related to the DFT geometry optimized atomic structure allowed to explain the yellow-green color of the powder, with two absorption bands centered at 2.2 and 3 eV. After analyzing the DFT data, these two bands appear to be the consequence of optical transitions from $V(3d_{xy})$ to $V(3d_{xz}, 3d_{yz})$ states. In addition, using the same approach (GGA+U with $U_{eff} = 2$ eV), magnetic spin exchange interactions in $VO(C_6H_5COO)_2$ have been estimated. Values of $J_{intra} = -171.9$ K and $J_{inter} = -0.2$ K, confirming that only intrachain interactions are relevant to describe the 1D character of the related magnetic structure.

Acknowledgment. Financial support from ETH Zürich is gratefully acknowledged. We express our gratitude to Prof. Robert Schlögl and Dr. Dang Sheng Su from the Fritz-Haber-Institute (FHI) in Berlin for the use of the

electron microscope. M.C. thanks the Alexander von Humboldt Foundation for supporting her research stay in Germany, the Natural Science Foundation Council of China (NSFC) (20771022), and the Program for New Century Excellent Talents in University.

Supporting Information Available: Figures S1−S4, Tables S1−S2 (PDF); two crystallographic information files (CIF), one deduced from the powder data and another deduced from the geometry optimization. This material is available free of charge via the Internet at http://pubs.acs.org.